



# Phased Array Feed Experiments and Galactic HI Observations

B. Liu<sup>1,2</sup>, H. W. Xi<sup>1,2</sup>, D. J. Ding<sup>1,2,3</sup>, Z. W. Wang<sup>1,2</sup>, S. H. Yu<sup>1,2</sup>, Y. Zhu<sup>1,2</sup>, L. Yu<sup>1,2</sup>, X. Zhang<sup>1,2</sup>, J. L. Li<sup>1,2</sup>, L. J. Liu<sup>1,2</sup>, Q. Su<sup>1,2</sup>,  
Y. Wu<sup>4</sup>, C. J. Jin<sup>1,2</sup>, and B. Peng<sup>1,2</sup>

<sup>1</sup>National Astronomical Observatories, Chinese Academy of Sciences, Beijing 100101, China; [pb@nao.cas.cn](mailto:pb@nao.cas.cn)

<sup>2</sup>Key Laboratory of Radio Astronomy and Technology, Chinese Academy of Sciences, Beijing 100101, China; [cjjin@nao.cas.cn](mailto:cjjin@nao.cas.cn)

<sup>3</sup>School of Astronomy and Space Science, University of Chinese Academy of Sciences, Beijing 100049, China

<sup>4</sup>The 54th Research Institute of China Electronic Technology Group Cooperation, Shijiazhuang 050081, China

Received 2023 April 28; revised 2023 May 23; accepted 2023 May 25; published 2023 July 11

## Abstract

The Phased Array Feed (PAF) is considered as one of the next generation receivers for radio telescopes, which can significantly enlarge the instantaneous Field-of-View of large aperture single dish radio telescopes and enable more flexible observing configurations. Study efforts on PAF development for radio telescopes have been made for more than two decades and have become more and more applicable. We report the development of an ambient-temperature 19 element *L*-band PAF system and the experimental results including its far field beam pattern and system temperature measurement, which achieve the expectations. Implementing the aperture array beam-forming method, we demonstrate a wide-field Galactic HI observations in the radio camera mode. The results indicate that this system might be applicable for strong Galactic transient detections. This system could be directly equipped to large telescopes like the Five-hundred-meter Aperture Spherical radio Telescope (FAST) and FAST array in the future.

*Key words:* instrumentation: detectors – techniques: imaging spectroscopy – line: profiles

## 1. Introduction

With the technology development, radio astronomy has entered the era of large surveys, in which telescopes with high-sensitivity and wide Field-of-View (FoV) are essential. Equipped with the traditional receiving system, radio telescopes with large apertures, like the Five-hundred-meter Aperture Spherical radio Telescope (FAST), are proficient in weak signal discoveries. However, high sensitivity comes with small FoV, thus the survey speed of such telescopes is quite limited. A telescope with the modern phased-array feed receiver can electronically form multiple far-field beams simultaneously to increase the instantaneous FoV without loss of sensitivity.

Several major instrument development projects are underway worldwide concentrating on the development of Phased Array Feeds (PAFs), among which there are for large single dishes such as the focal *L*-band array (FLAG) and the Advanced *L*-band Phased Array Camera for Astronomy (ALPACA) for the Green Bank Telescope (Warnick et al. 2018; Vishwas et al. 2022), “Rocket” PAF for the Parkes Telescope (Dunning et al. 2016), as well as projects for Effelsberg telescope in Germany (Deng et al. 2018) and Lovell telescope at Jodrell Bank Observatory (Zhang et al. 2019). In the mean time, PAF receivers are also implemented by interferometry including the Westerbork Synthesis Radio Telescope (WSRT, van Cappellen et al. 2022) and the

Australian SKA Pathfinder Telescope (ASKAP, Chippendale et al. 2010) and have shown great potential for large surveys.

With a PAF-based system, one can create radio images from the complete coverage of FoV made by the multiple simultaneously formed beams. Other advantages of a radio telescope equipped with the PAF receiver are configurable beam shapes that adapt to the noise and radio frequency interference (RFI) environment, and observing with electronic steering beams within the FoV.

The team of Joint Laboratory for Radio Astronomy Technology (JLRAT) at National Astronomical Observatories of Chinese Academy of Sciences (NAOC) has been working on the development of PAF instrument over a decade. Many research efforts have been concentrated on the feed array optimization, as early experimental verification of the 19 element array and 31 element array have been designed and manufactured. Recently, we assembled a PAF receiver based on our 19 element feed array by using commercial discrete electronic devices which are available with good performance and quality in the market. The PAF is designed to be fully functional for astronomical experiments. In order to test the basic system properties and further understand how it works in astronomical observations, we also deployed observational experiments at Huairou Solar Observing Station in Beijing. In the experiments, the feed array is placed on the ground with its bore-sight pointed to the zenith, observing the sky as an

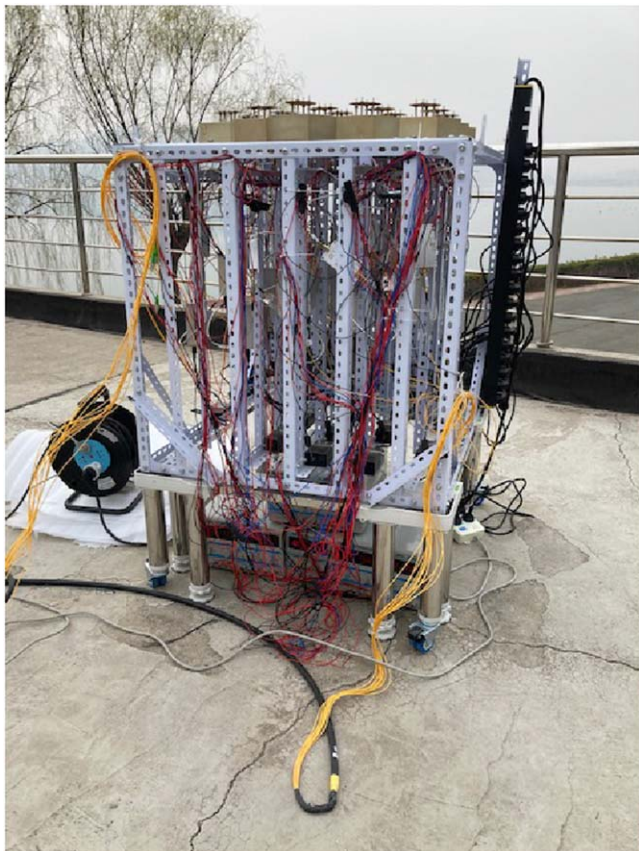


**Figure 1.** The picture of the PAF system at Huairou Solar Observing Station.

aperture array. Figure 1 presents the picture of the PAF system during an observation at Huairou Solar Observing Station.

In this paper, we will introduce the schematics of the PAF receiver and present the results of the system experiments and the observed HI images of the Milky Way. Section 2 shows the analog frontend and digital backend systems along with the calibration and beam-forming procedures. Section 3 demonstrates the experimental results including the RFI situation, beam pattern, and system temperature. Section 4 presents the details of the Galactic HI observation with the PAF system and the HI images as the results. Our work is summarized in Section 5.

## 2. The PAF System

### 2.1. The Analog Frontend

We use the 19 element room temperature PAF receiver designed by the JLRAT to make the experiments and HI observations. The PAF is composed of 19 hexagonal arranged back-cavity dipoles with element spacing  $0.65\lambda$  ( $\sim 140$  mm), and its bandwidth is 1.05–1.45 GHz with dual polarization (Wu et al. 2013). The maximum radial distance from the center of

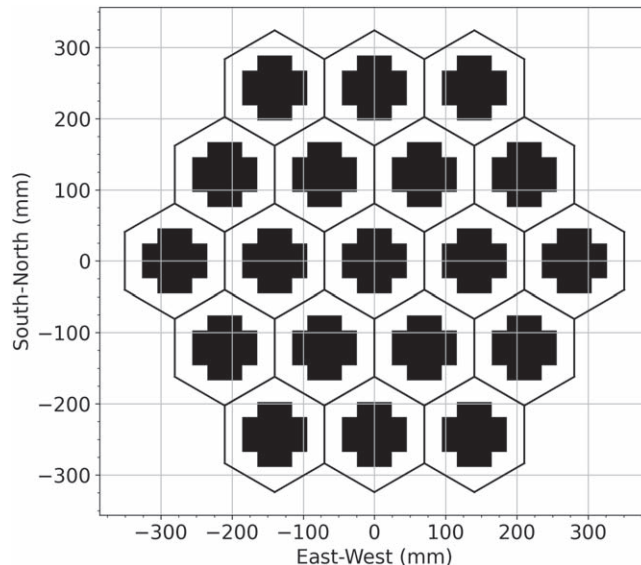


**Figure 2.** The sketch diagram of the feed array. The “+” signs in black show the size of the dipoles.

the array is 350 mm. The array arrangement is shown in Figure 2.

After received by the feed array, the signal from each element is transmitted to the digital backend through the analog frontend, which is assembled based on the commercial discrete electronic devices (Figure 1). The analog chain is illustrated in Figure 3, in which the signals are amplified and filtered by two stages of low noise amplifiers (LNAs) and bandpass filters (BPFs). The gain and noise figure (NF) of the first stage LNA are about 20 and 0.6 dB, while the gain and NF of the second LNA are about 25 and 1.5 dB. The frequency range of two BPFs is 1360–1440 MHz. This is to avoid RFI as much as possible and keep the bandpass clean. After being adjusted into proper power level, the radio frequency (RF) signal is converted and transmitted through Radio Frequency over Fiber (RFoF) module to another BPF and then down-converted to intermediate frequency (IF) by a mixer with local oscillator (LO) at 1360 MHz. The signals then go through a lowpass filter (LPF) of DC-70 MHz and are amplified before it is digitized. Note that the RFoF module have an ultra-high noise figure, so that at least 60 dB amplification is required to suppress the noise from the RFoF module. It is important to monitor the strength of signals in each channel in case of the power overflow and the nonlinear effects in each level element. Screened wires and elements are used to prevent the leak of radio signals and the crosstalk in each channel.

### 2.2. The Digital Backend

The backend of our PAF system is designed to digitize the IF signal with 100 MHz bandpass and store the baseband data to

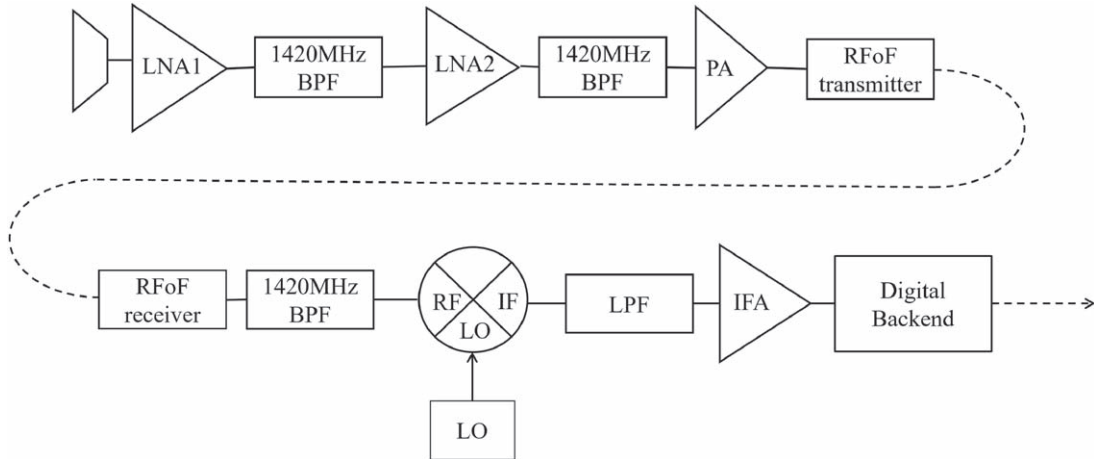


Figure 3. The sketch of analog frontend.

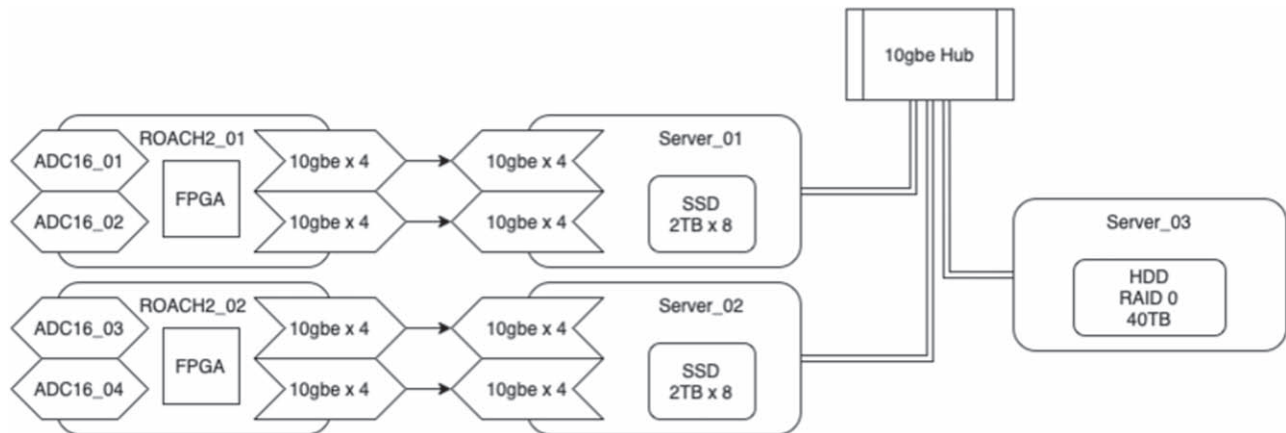


Figure 4. The overview of the PAF backend.

the disks, which is then processed in off-line mode including channelization, calibration, and beam-forming. This system contains two ROACH2<sup>5</sup> boards and three high-performance computers (HPCs), which provide the full capability of recording and processing 64 analog signals. Figure 4 shows the overview of the backend system.

On the ROACH2 board, two ADC cards are equipped, each of which is used to digitize 16 RF signals with a 240 MHz sampling rate and sampling bit width. Thus, the two ROACH2 board systems could digitize a total of 64 IF signals under the current configuration with the baseband data rate of 240 Mega-samples per second (Msps) for one analog path. Each four sampled signals are packaged and sent to the HPC through one 10gbe Ethernet port with a total data rate of  $960 \text{ MB s}^{-1}$ . Two  $10\text{gbe} \times 4$  Ethernet cards are equipped on both the ROACH2

boards and the data recording HPCs in order to transfer the baseband data to the servers.

A pipeline has been developed to process the recorded baseband data step by step in offline mode, including channelization, calibration, and beam-forming. We implement the Poly-phase Filter Bank algorithm for the channelizer in the pipeline. Eight taps and 4096 channels are configured to produce a 120 MHz bandpass with a frequency resolution of  $\sim 29.297 \text{ kHz}$  and negligible channel leakage. The corresponding velocity resolution at 1420 MHz is then  $6.2 \text{ km s}^{-1}$ . Details of calibration and beam-forming are described as follows.

### 2.2.1. Calibration

A calibration procedure is designed to calibrate the phase and amplitude of different signal paths introduced by the electronics and ADCs. We calibrate the system by injecting a noise signal to the LNAs of the frontend and recording the data in the backend.

<sup>5</sup> <https://casper.astro.berkeley.edu/wiki/ROACH2>

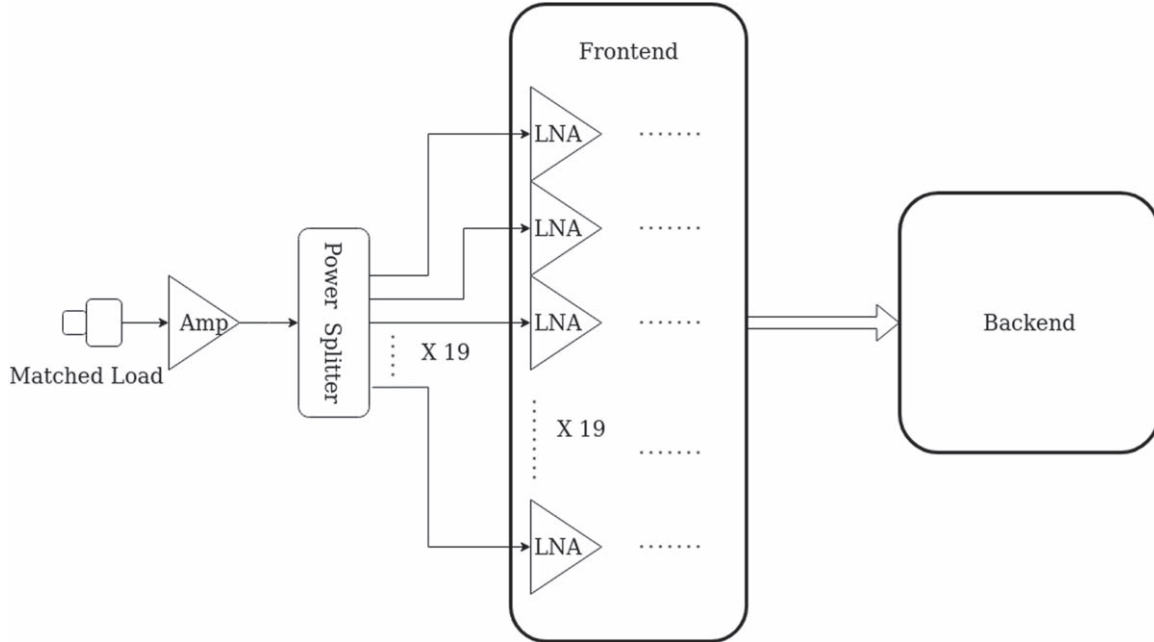


**Figure 5.** The configuration of system calibration using white noise.

The white noise signal is generated by a  $50\Omega$  matched load, and then amplified and equally divided into 19 paths, and then routed to the LNAs by coaxial cables with exactly the same length. The configuration of the procedure is illustrated in Figure 5.

The baseband data of the test is recorded by the digital backend, and then processed for our two-step calibration pipeline. First, we chose the signal from the central element as the reference and then calculate the cross-correlation of all others and the reference signal, from which the relative time delay in a unit of digital samples is obtained. Second, the baseband signals are channelized after their time delays are corrected and their complex ratio to the reference signal is calculated over all the frequency channels. By averaging the complex ratio over observing time and performing a linear fitting, we obtain the phase and amplitude calibration factors, which, along with the time delays, are recorded and will be applied to other data from regular observations.

### 2.2.2. Beam-forming

As mentioned previously, instead of being equipped with a dish antenna and working as a real PAF, the feed array works as an aperture array, being placed on the ground with its bore-sight pointed to the zenith. Therefore, we implement the beam-forming algorithm for plane wave observation rather than focal plane detection.

After calibration, the signals from different elements should be in the same amplitude with the same phase. To form a beam to the expected direction, one only needs to change the phase

angle of the signal according to the observing direction and the baseline between this element and the reference one. To create the map of the sky, we formed beams with  $5^\circ$  steps in both azimuth and elevation axis, with a  $60^\circ$  FoV from  $30^\circ$  to  $90^\circ$  in elevation. The results will be shown in the following sections.

## 3. System Experiments

### 3.1. Radio Frequency Interference

The bandpass of the PAF system is designed relatively narrow to avoid strong RFIs in the environment, since no radio-quiet zones are actually reachable for this work. Even so, when being carried out at the headquarters of NAOC in Beijing, the first experiment was corrupted by severe RFIs in the frequency band 1460–1490 MHz, transmitted by wireless devices of the Internet of Things (IoT), since the artificial signals can easily cause the LNAs to get saturated. In an effort to circumvent severe RFIs, we deployed the following PAF experiments and observations at Huairou Solar Observing Station located in the suburban district of Beijing, where the RF circumstance is rather quiet.

However, weak RFIs appear when the strong RFIs are eliminated. As an example, the RF bandpass of the central element is given in Figure 6. The left side plot shows the original spectrum with severe wide-band RFIs including 1366–1373 MHz, 1375 MHz, 1400–1408 MHz, 1413–1417 MHz, and 1425 MHz, which were then identified from a DC power supplier. Also, a narrow spike at 1420 MHz was identified from the CPU of the spectrum analyzer which was used to monitor the RF signal. The observation went on after the spectrum analyzer was

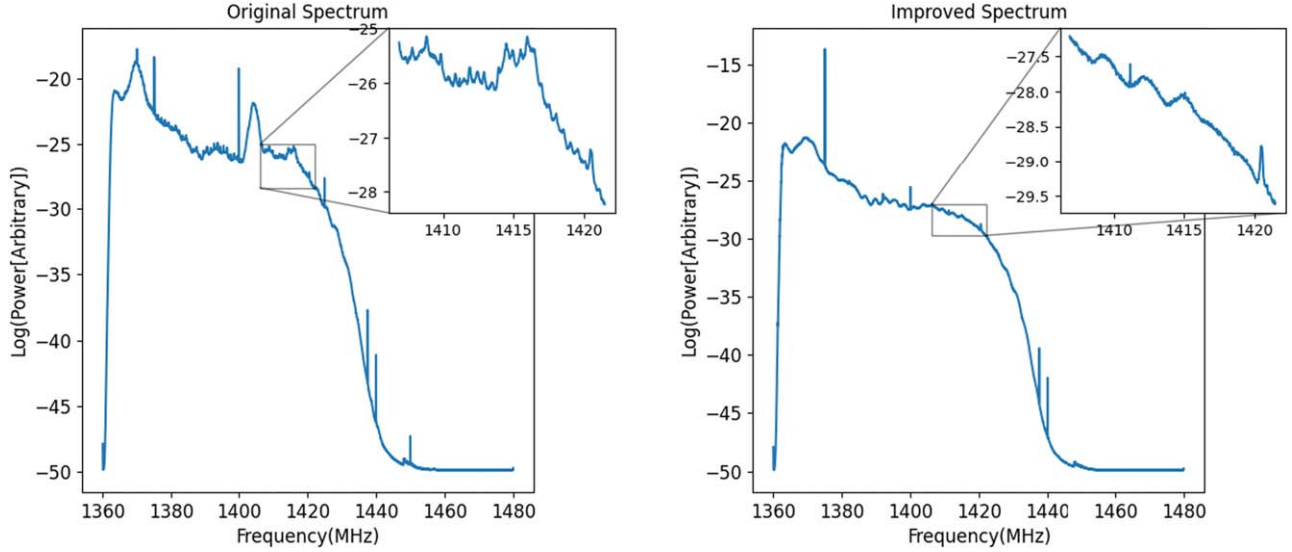


**Figure 6.** An example of the RF bandpass and RFIs from the central element. The left panel shows spectrum affected by the DC power supplier, within which the H I line profile can be severely corrupted. The right panel is the spectrum after the DC device introduced RFIs were eliminated.

powered off and the power supplier was replaced. Moreover, some quasi-periodic ripples like standing waves exist in the baseline. As a comparison, the improved spectrum is shown in Figure 6 (right).

### 3.2. Beam Pattern

One of the important parameters of PAF is synthesis beam pattern. Considering the projection of a round aperture, it has elliptical shape with major axis along offset direction from main optical axis in theory. Special case, the synthesis beam becomes a round shape at main optical axis direction. Hence, we can use the following relation to model the beam size with elliptical shape.

$$a = \frac{b}{\cos(ZA)} \quad (1)$$

where  $a$  and  $b$  are the FWHMs along major and minor axes of the synthesis beam, and  $ZA$  is the offset angle of the synthesis beam from the main optical axis. In general, it can be derived by observing a distant compact source, e.g., a celestial object or a distant artifact source. In reality, it is much easier for us to use an artifact source to measure the beam shape at different offset angle from the main optical axis. Considered the PAF was fixed on the ground during the observation, the offset angle from the main optical axis is also the zenith angle of the PAF.

In order to derive the beam pattern, a bipolar antenna was placed at a distance of 5 meters (larger than the far field distance<sup>6</sup> of  $\frac{2D^2}{\lambda} \sim 4$  m at 21 cm for our PAF receiver) with

different zenith and azimuth angle. The antenna was along the polarization channel of PAF we used. The optical path difference between central and outer element is about 5.9 mm (equivalent phase difference of  $10^\circ$  for 21 cm, the characteristic wavelength at  $L$ -band) at  $ZA = 0^\circ$ , which is negligible in our beam forming procedure. A sine wave at 1.4215 GHz was generated by a signal generator from *RF explorer*,<sup>7</sup> and was emitted by the bipolar antenna. Figure 7 shows the intensity maps with the bipolar antenna at different azimuth and zenith angle ( $Az, ZA$ ): left panel ( $\sim 0^\circ, \sim 0^\circ$ ), middle panel ( $\sim 270^\circ, \sim 45^\circ$ ), and right panel ( $\sim 180^\circ, \sim 50^\circ$ ). It clearly shows the synthesis beam having round shape at the zenith, and elliptical shape at other zenith angle. For simplicity, we ignored the effects from side-lobes, and used two-dimensional Gaussian function with constraint of Equation (1) to fit the maps. The modeled beam shapes are given by the white circles with plus signs at the centers. The best fit parameters are given in Table 1. Figure 8 shows the normalized power as a function of  $ZA$  at different  $Az$ , which was derived by relocating the map center (left panel of Figure 7) to the best fit position of the synthesis beam. The side-lobes have normalized power below  $\frac{1}{10}$ , which is negligible for our Galactic H I observations (see Section 4).

Figure 9 shows the variation of beam major ( $a$ ) and minor ( $b$ ) axis along the zenith angle. The variation trend is consistent with our expectation,  $a$  increasing along zenith angle while  $b$  nearly constant. We use Equation (1) and  $b = \text{constant}$  to

<sup>6</sup> <https://www.everythingrf.com/rf-calculators/antenna-near-field-distance-calculator>

<sup>7</sup> <http://j3.rf-explorer.com/40-rfe/article/124-rf-explorer-signal-generator>

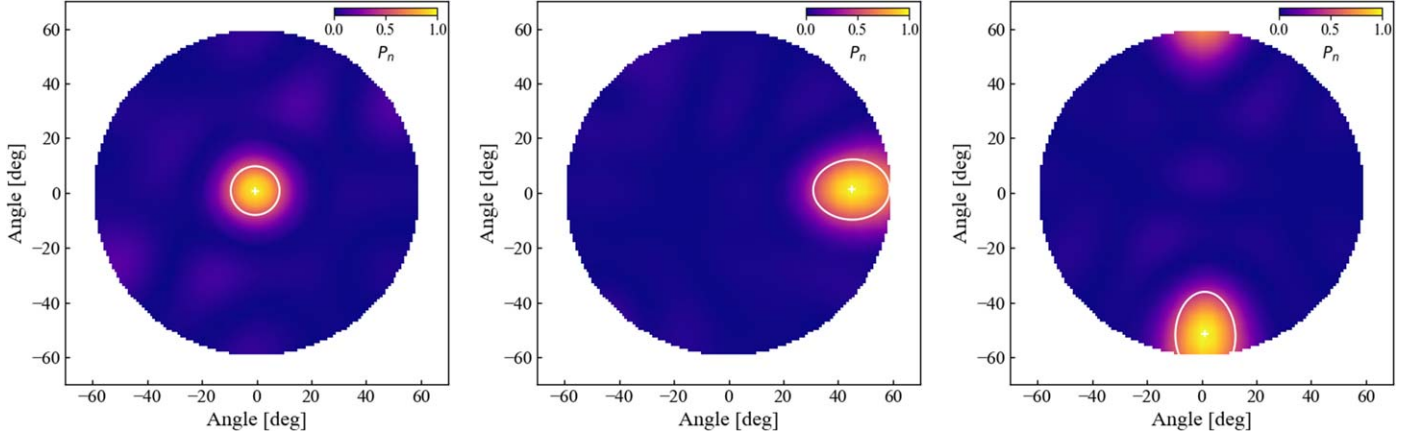


**Figure 7.** Normalized intensity maps of point sources at different azimuth and zenith angle (Az, ZA): left panel ( $\sim 0^\circ$ ,  $\sim 0^\circ$ ), middle panel ( $\sim 270^\circ$ ,  $\sim 45^\circ$ ), and right panel ( $\sim 180^\circ$ ,  $\sim 50^\circ$ ). The beam shape has a round shape at the zenith, and elliptical shape at other zenith angle. The white circles are the best fit by two-dimensional Gaussian function. The plus signs indicate the centers of the best fit beams.

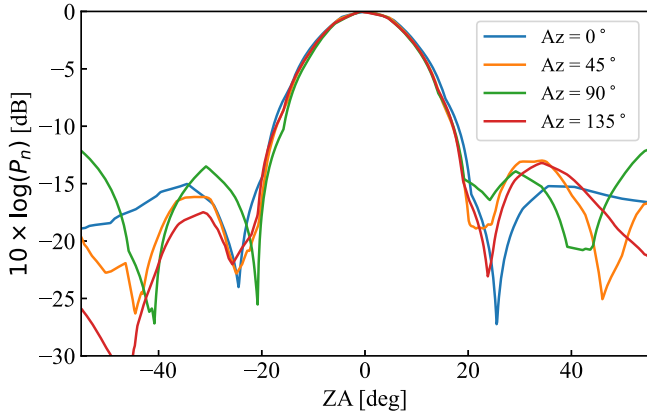


**Figure 8.** The power pattern derived from the left panel of Figure 7 for  $Az = 0^\circ, 45^\circ, 90^\circ, 135^\circ$ . The center is relocated at the best fit position from two-dimensional Gaussian function.  $P_n$  is the normalized power.

**Table 1**

Best Fit Parameters of Beam Shape by a Two Dimensional Gaussian Function

Az (deg)	ZA (deg)	a (deg)	b (deg)
33.68 (1.29)	0.96 (0.02)	17.83 (0.01)	17.83 (0.04)
271.50 (0.02)	44.92 (0.02)	27.96 (0.01)	19.80 (0.02)
181.53 (0.06)	51.37 (0.11)	30.60 (0.07)	19.10 (0.11)

**Note.** The first two columns gives the azimuth and zenith angle of the best fit beam centers. The third and fourth columns are the FWHMs of the major and minor axis of the beams. The  $1\sigma$  uncertainties are given in the parentheses.

model the beam axes. The best fit model is given below.

$$\begin{cases} a = \frac{18^\circ 91}{\cos(ZA)} \\ b = 18^\circ 91 \end{cases} \quad (2)$$

where  $a, b$  are the major and minor axes of synthesis beam, and ZA is zenith angle. The beam model will be used to mock H I sky for comparison (see Section 4.2).

### 3.3. System Temperature

The beam equivalent system noise temperature  $T_{\text{sys}}$  can be expressed as (Warnick & Jeffs 2008; Landon et al. 2010)

$$T_{\text{sys}} = \eta_{\text{rad}}(T_{\text{sky}} + T_{\text{sp}}) + T_{\text{loss}} + T_{\text{rec}}, \quad (3)$$

where  $\eta_{\text{rad}}$  is the radiation efficiency of PAF and here we adopt  $\eta_{\text{rad}} = 1$ .  $T_{\text{sky}} = T_{\text{cmb}} + T_{\text{gb}} + T_{\text{atm}}$  is the sum of noise temperature in the main lobe caused by the cosmic microwave background (CMB) radiation  $T_{\text{cmb}} \approx 2.73$  K (Fixsen 2009), galactic background  $T_{\text{gb}} \approx 1$  K, and atmospheric noise  $T_{\text{atm}}$  (here neglected temporarily).  $T_{\text{sp}} \approx 2$  K is the equivalent spillover noise temperature.  $T_{\text{loss}} \approx 14$  K is the loss noise including resistive losses in the antenna, cables, and connectors ahead of the LNA, dominated by the coaxial cable loss.  $T_{\text{rec}}$  is the beam equivalent receiver noise temperature which is obtained from our experiments.

Assuming that there is perfect impedance match between the element antenna and the contiguous LNA, and the noise temperature is proportional to the corresponding power received by PAF, the PAF receiver noise temperature  $T_{\text{rec}}$  can be calculated by

$$\frac{T_{\text{rec}} + T_{\text{sky}} + T_{\text{loss}}}{T_{\text{rec}} + T_{\text{iso}} + T_{\text{loss}}} = \frac{\omega^H \mathbf{R}_{\text{cold}} \omega}{\omega^H \mathbf{R}_{\text{hot}} \omega}, \quad (4)$$

where  $\mathbf{R}_{\text{cold}}$  and  $\mathbf{R}_{\text{hot}}$  are the voltage noise covariance matrices recorded in the backend when the PAF pointed to cold sky and was shielded by  $\sim 1.0 \text{ m} \times 1.0 \text{ m}$  sheet of RF absorber,  $\omega$  and  $\omega^H$  the the weighting factor matrix of array dipole elements and its conjugate matrix. In our measurements, we take into consideration that  $T_{\text{sp}}$  is included in  $T_{\text{rec}}$ , because  $\mathbf{R}_{\text{cold}} = \mathbf{R}_{\text{rec}} + \mathbf{R}_{\text{sky}} + \mathbf{R}_{\text{loss}} + \mathbf{R}_{\text{sp}}$  where  $\mathbf{R}_{\text{rec}}$ ,  $\mathbf{R}_{\text{sky}}$ ,  $\mathbf{R}_{\text{loss}}$ , and  $\mathbf{R}_{\text{sp}}$  are the receiver, sky, antenna resistive loss, and spillover noise covariance matrices, respectively.

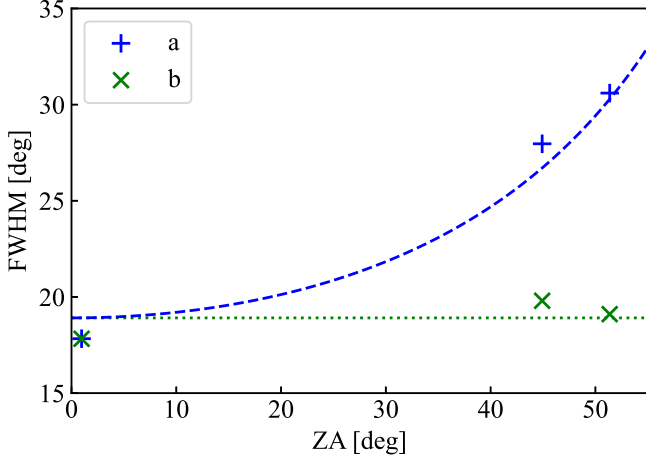


**Figure 9.** The variation of beam major and minor axes along zenith angle. The best fit lines (Equation (2)) are indicated by the blue dashed and green dotted lines.

In addition to the above noise sources, other noise signals, for instance, reflected space electromagnetic waves by neighboring antennas or return waves due to the mismatch in the radio links can also excite the array antennas and enter into the receiver chains of PAF, resulting in variation of receiver noise temperature. This is the so-called mutual coupling effect. Correspondingly, we call the excitation of the array antennas by itself as self-coupling. In the presence of the mutual coupling, off-diagonal terms in  $\mathbf{R}_{\text{rec}}$  are non-zero. The measured noise temperature due to the mutual coupling is included in the equivalent receiver noise temperature. We can estimate the mutual coupling noise by separating the diagonal and off-diagonal terms in  $\mathbf{R}_{\text{rec}}$ .

Throughout the paper, we calculate the noise temperature  $T_{\text{noise}}$  by adopting isotropic temperature of 283 K during the observations. Figure 10 illustrates the receiver noise temperature with ( $T_{\text{rec}}$ , black line) and without the mutual coupling noise temperature ( $T_{\text{rec}} - T_{\text{mc}}$ , red line) as a function of the radio frequency. The frequency band is from 1418 to 1423 MHz with 171 channels, so the bandwidth for a channel is  $\sim 29$  kHz. From the figure, we see that  $T_{\text{rec}}$  is from  $\sim 60$  K to  $\sim 150$  K across the frequency band, and the mutual coupling sometimes contributes considerably to the system noise temperature. The averaged system noise temperature and the main components over the frequency band 1418–1423 MHz (bandwidth 5 MHz) are listed in Table 2.

At frequency  $\sim 1420$  MHz with bandwidth  $\sim 29$  kHz, the arbitrary values of covariance of data (after calibration) for an isotropic source recorded by all element antennas in the PAF is  $33.65 \times 10^{-2}$ , while the arbitrary value of covariance of data (after calibration) for cold sky recorded by all element antennas is  $9.09 \times 10^{-2}$ . We obtain the noise temperature of PAF by Equation (4) at 1420 MHz (bandwidth 29 kHz) in our observations to be 83 K. In addition, the measured  $\omega^H \mathbf{R}_{\text{cold}} \omega$ ,  $\omega^H \mathbf{R}_{\text{hot}} \omega$  and the derived noise temperature ( $T_{\text{noise}}$ ) due to the self-coupling by center dipole, self-coupling by array dipoles

and total coupling (self- and mutual) by array dipoles are listed in Table 3, adopting equal weighting factor.

We can alternatively calculate the noise temperature due to the first stage LNAs and subsequent circuits by the cascaded noise factor formula

$$F_{\text{total}} = F_1 + \frac{F_2 - 1}{G_1} + \frac{F_3 - 1}{G_1 G_2} + \frac{F_4 - 1}{G_1 G_2 G_3} + \dots \quad (5)$$

where  $F_1, F_2, F_3$  denotes the noise factor of the first stage amplifier, second stage amplifier, third stage amplifier, and  $G_1, G_2, G_3$  the gain of each stage amplifier respectively. From the formula, we see that if the noise factor is sufficiently small or the gain is large, the noise temperature of a cascaded system is mainly dominated by the first stage LNA.

We used the ZX60-P162LN+ manufactured by Mini-circuits as the first stage LNA. It has a noise figure of 0.6 dB in room temperature and gain of  $\sim 20$  dB. The measured total equivalent noise figure using a noise source in front of the first level LNA is about 0.67 dB, which lead to a noise temperature of about 48 K. The gain, noise figure and noise temperature contribution of each amplifier (typical) is listed in Table 4. This result is approximately consistent with our noise temperature measurement of the center dipole and its corresponding circuit.

## 4. Galactic HI Observation

Hydrogen is the most abundant element in the universe. It has three forms: (1) ionized hydrogen (H II), (2) atomic hydrogen (H I) and (3) molecular hydrogen (H<sub>2</sub>). H I is the most common form in our Milky Way, and accounts for the majority of the interstellar medium (ISM) mass. It provides fuels to the star formation regions, therefore indirectly regulates the star formation rate (Sancisi et al. 2008). The prevalent property makes it an ideal tracer of large scale structures, e.g., filaments (Syed et al. 2022). The spatial distribution and velocity field of H I also enables the subtle studies on dynamics of the Milky Way, e.g., structure and rotation curve (Tavakoli 2012). The whole H I content in our Milky Way was first mapped by the Leiden/Argentine/Bonn (LAB) Survey (Kalberla et al. 2005), which combined the Leiden/Dwingeloo Survey (LDS, Hartmann & Burton 1997) on the northern sky and the Instituto Argentino de Radioastronomia Survey (IAR, Arnal et al. 2000; Bajaja et al. 2005) on the southern sky. The diffuse distribution in the whole sky makes it an ideal target for testing the PAF. Considered the PAF having a large FoV, it is able to map the distribution of the Galactic H I contents in a short integration time. It also allows us to trace the movement of the Milky Way in the sky by H I contents if the observation could last a long time.

### 4.1. Observation

The observation was performed at Huairou Solar Observing Station, which is located at longitude of  $116^\circ 35' 39''$  E, latitude of  $40^\circ 18' 59''$  N, and altitude of 57.9 m. The zero-point of the

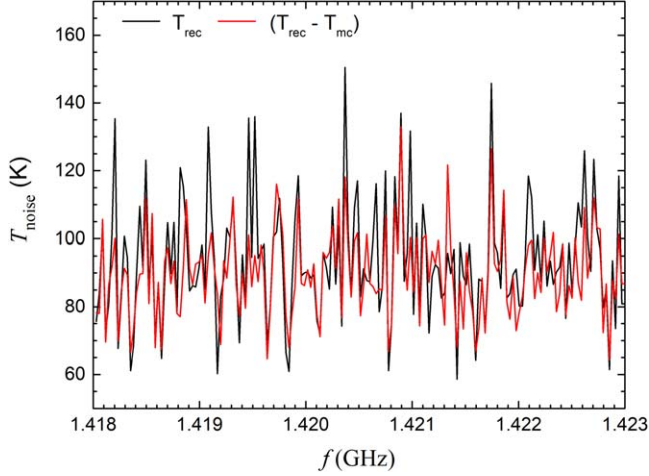


**Figure 10.** The noise temperature ( $T_{\text{noise}}$ ) as a function of the radio frequency. Black line: the receiver noise temperature  $T_{\text{rec}}$  adopting equal weight beam-forming factor for amplitude and environment temperature of 283 K. Red line: same as the black line except excluding the noise temperature due to the mutual coupling, i.e.,  $T_{\text{rec}} - T_{\text{mc}}$ . The frequency band is from 1418 to 1423 MHz with 171 channels, so the bandwidth of a channel is  $\sim 29$  kHz.

**Table 2**

Averaged System Noise Temperature and the Main Components over the Frequency Band 1418–1423 MHz (Bandwidth 5 MHz) in our Observations, Adopting Environment Temperature of 283 K and Equal Weighting Factor

$T_{\text{rec}}$	$93 \pm 17$ K (Measured, Including $8 \pm 8$ K of $T_{\text{mc}}$ )
$T_{\text{sky}}$	3.73 K (estimated)
$T_{\text{loss}}$	14 K (estimated)
$T_{\text{sp}}$	2 K (estimated)
$T_{\text{sys}}$	$112.73 \pm 17$ K

**Table 3**

The Measured Noise Covariance Matrices for Cold Sky ( $\omega^H \mathbf{R}_{\text{cold}} \omega$ ) and an Isotropic Radio Frequency Absorber ( $\omega^H \mathbf{R}_{\text{hot}} \omega$ ), and the Derived Noise Temperature ( $T_{\text{noise}}$ ) Due to the Self-coupling by Centre Dipole, Self-coupling by Array Dipoles and Total Coupling (Self-and Mutual) by Array Dipoles at Frequency of  $\sim 1420$  MHz (Bandwidth  $\sim 29$  kHz), Adopting Environment Temperature of 283 K and Equal Weighting Factor

	$\omega^H \mathbf{R}_{\text{cold}} \omega$	$\omega^H \mathbf{R}_{\text{hot}} \omega$	$T_{\text{noise}}$
self-coupling by center dipole	$0.77 \times 10^{-3}$	$3.67 \times 10^{-3}$	54 K
sum of self-coupling by array dipoles	$2.06 \times 10^{-2}$	$7.96 \times 10^{-2}$	77 K
sum of self- and mutual coupling by array dipoles	$9.09 \times 10^{-2}$	$33.65 \times 10^{-2}$	83 K

PAF azimuth angle was adjusted toward geographic north by using a compass. A spirit level was employed to adjust the orientation of the PAF receiver plane to the zenith. The noise from a resistor was simultaneously injected to the 19 systems from the first LNAs to calibrate whole system (see Section 2.2.1 for details). The local oscillator was set to 1.36 GHz,

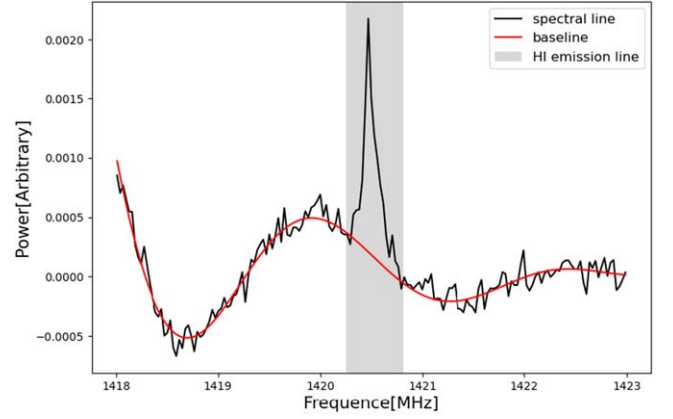


**Figure 11.** The spectrum with a baseline fitted by Equation (6). The gray area indicates the signal of 21 cm emission line from the Galactic H I. The red line represents the best fit of the baseline.

**Table 4**

The Parameters of the Amplifier used in this Experiment and its Contribute to Total NF and  $T_{\text{rec}}$

Name	Gain	Noise Figure	Contribute to NF	Contribute to $T_{\text{rec}}$
ZX60-P162LN+	20 dB	0.6 dB	0.6 dB	43 K
ZRL-2150+	25 dB	1.5 dB	0.053 dB	4 K
ZFL-2500VHX+	20 dB	5.5 dB	0.0013 dB	0.15 K

which is close to the frequency of H I 21 cm emission line ( $\sim 1.42$  GHz). Two ROACH2 were employed to record the data from 19 elements with sampling rate of 240 Msps. The channelization and beam forming were performed offline (see Section 2.2.2 for details). The 120 MHz bandwidth (corresponding to 1.36–1.48 GHz before down sampling) was split by 4096 channels, which gives a frequency resolution of 29.3 kHz (velocity resolution of  $6.2 \text{ km s}^{-1}$  at  $z = 0$ ). The spectra were generated with azimuth step of  $5^\circ$  and zenith step of  $5^\circ$  in beam forming procedure.

Considered the limited storage for the baseband data, the observations were automatically carried out with an integration time of 10 s every half an hour from 2023 March 18 to 2023 March 19. The data allow us to trace the movement of our Milky Way.

## 4.2. Results

A three-dimensional cube (space-space-frequency) was generated for each observation during the beam forming procedure. Due to the blockage from the environment, the cube only covers  $\text{ZA} \leq 60^\circ$  with  $0^\circ \leq \text{Az} < 360^\circ$ . The spectra show a standing wave with a period of  $\sim 2$  MHz. The standing wave becomes stronger at large zenith angle. Due to the existence of RFIs and variation of standing wave amplitude, the baseline

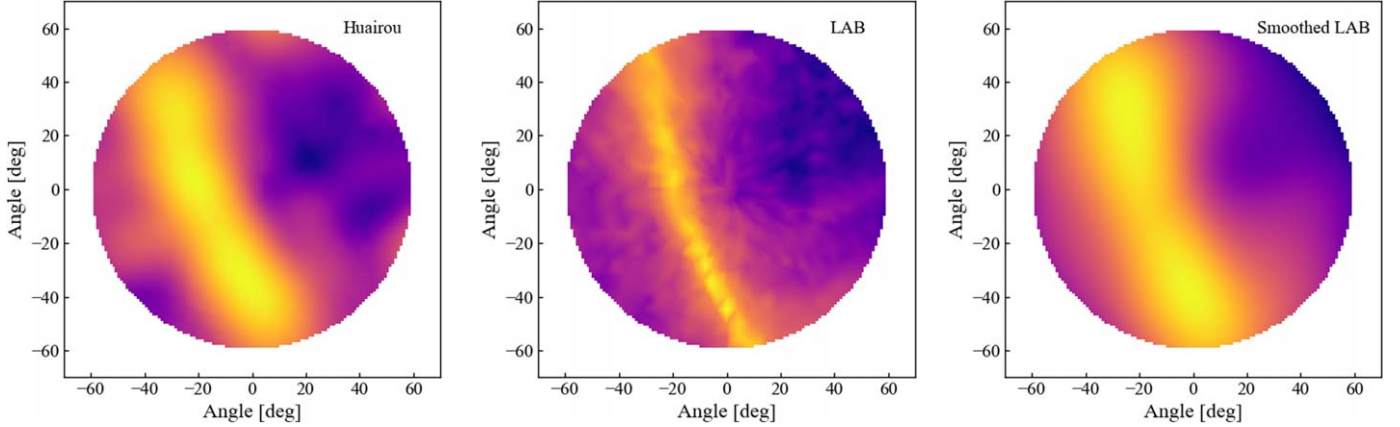


**Figure 12.** The distribution of H I content in Milky Way at 23:12:38 (UTC time) on 2023 March 18. Left panel: integration map from PAF observation. Middle panel: integration map from LAB data. Right panel: integration map from LAB data smoothed by PAF synthesis beam.

cannot be flattened by simply removing the out layers of FFT components. The polynomial function also cannot model the baseline properly. Hence, we use the following formula to fit the baseline, which consists of a sine function and a polynomial function. The sine function has a polynomial function as its amplitude.

$$P(\nu) = f_1(\nu)\sin(\omega\nu + \phi) + f_2(\nu) \quad (6)$$

where  $P$  is the power in arbitrary unit,  $\nu$  is frequency in unit of MHz,  $\omega$  and  $\phi$  are the angular frequency and phase of the sine function,  $f_1$  and  $f_2$  are two third-order polynomial functions. As an example, Figure 11 shows a spectrum with a baseline fitted by Equation (6). We can see the baseline can be well estimated by the function.

The integration map was derived after removing the baseline. Although we measured the main beam pattern, the response from side-lobes is still unclear. Here, we did not remove the side-lobe effect in the integration time. As an example, Figure 12 shows the integration map in logarithm scale from the observation performed at 23:12:38 (UTC time) on 2023 March 18. The Galactic plane is obviously detected as a bright band from south to northeast in the map. We also generated the H I distribution in the sky at the same time and location by using the LAB data. The LAB survey has spatial resolution of  $0.6^\circ$ , which is much higher than ours ( $\sim 19^\circ$  at the zenith). For comparison, we used the model beam of PAF (Equation (2)) to smooth the LAB data to mock PAF observation. Note that the side-lobe is not taken into account. The maps from LAB and smoothed LAB data are also shown in Figure 12. The map from PAF observation is consistent with mock H I sky from the LAB data. Considered the large beam size of PAF, the small scale structure in the left panel is caused by noise. All the integration maps from 24 hr observations are given in the Appendix to show the movement of the Galactic H I contents in the sky (see Figure A1).

## 5. Summary

We have reported the development of an ambient-temperature 19 element  $L$ -band PAF system and the implementation of calibration and beam-forming algorithms. The experimental results of the far field pattern tests and system noise temperature measurements are presented, which achieve the expectations. During these experiments, we have also identified RFIs from the test instruments and applied baseline fitting methods for standing wave ripples removal in the frequency bandpass. Adopting the aperture array beam-forming method, we have demonstrated wide-field Galactic H I observations in the radio camera imaging mode, and it has been shown that this PAF system has great potential for strong Galactic transient detection when directly observing as a wide FoV radio camera. These experimental results indicate that the PAF system is fully functional, and may be directly equipped to large telescopes like FAST and FAST array in the future.

## Acknowledgments

We thank the staff at Huairou Solar Observing Station, NAOC for their strong support during our experiments. This work is supported by the National Key R&D Program of China under grant No. 2018YFA0404703, and the Open Project Program of the Key Laboratory of FAST, NAOC, Chinese Academy of Sciences.

## Appendix H I Observation in 24 Hr

Figure A1 presents the H I integration maps of 24 hr observations, which show the movement of the Galactic H I contents in the sky.

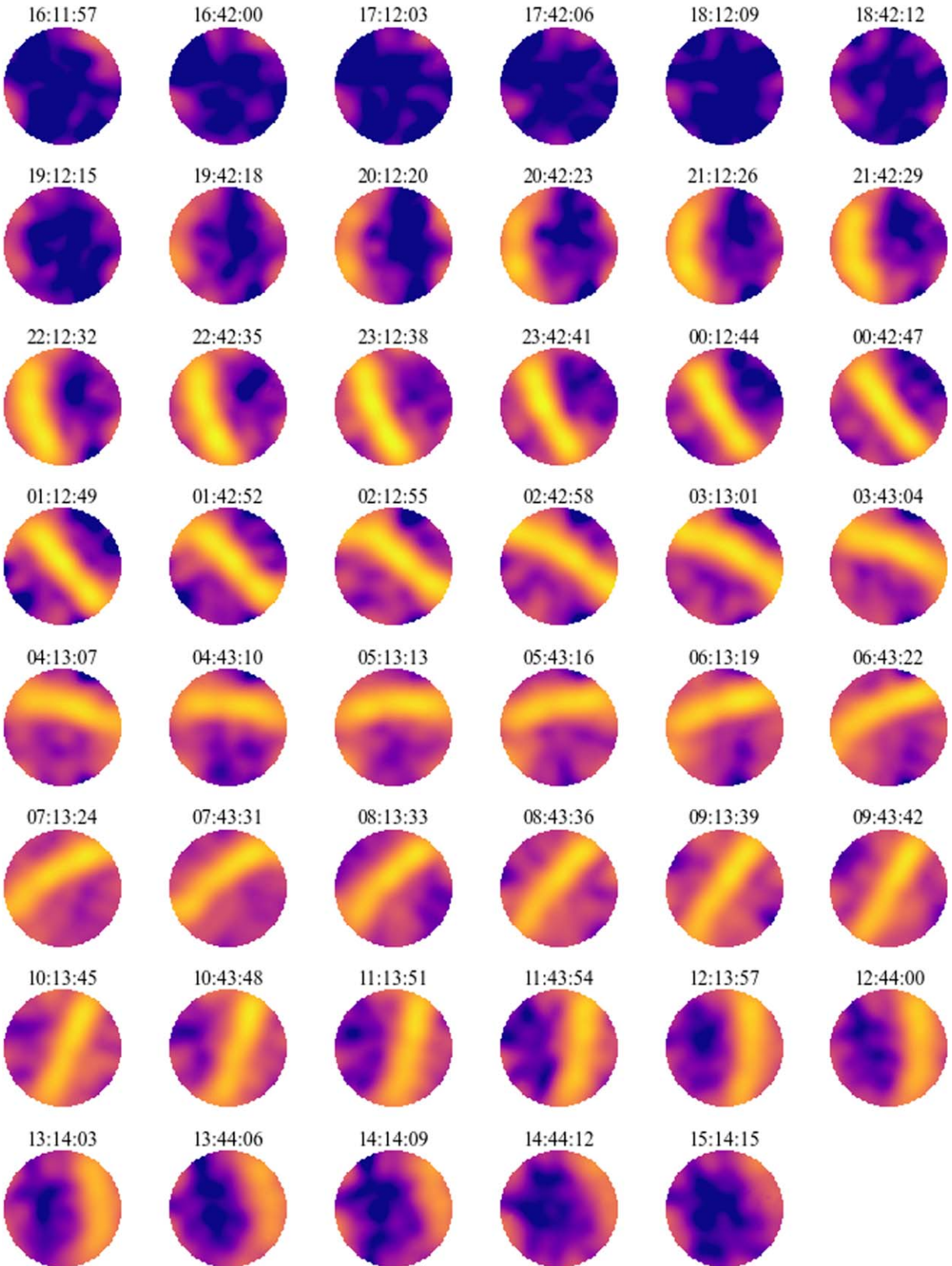


**Figure A1.** The integral H I maps of 24 hr observations from 2023 March 18 to 2023 March 19. The UTC time is given on top of each map. The Galactic plane was detected as a bright band in the maps.

## References

- Arnal, E. M., Bajaja, E., Larrarte, J. J., Morras, R., & Pöppel, W. G. L. 2000, *A&AS*, **142**, 35
- Bajaja, E., Arnal, E. M., Larrarte, J. J., et al. 2005, *A&A*, **440**, 767
- Chippendale, A., O'Sullivan, J., Reynolds, J., et al. 2010, in 2010 IEEE International Symposium on Phased Array Systems and Technology (Waltham, MA: IEEE), 648
- Deng, X., Chippendale, A., Barr, E., et al. 2018, in Pulsar Astrophysics the Next Fifty Years, ed. P. Weltevrede et al., Vol. 337 (Cambridge: Cambridge Univ. Press), 330
- Dunning, A., Bowen, M. A., Hayman, D. B., et al. 2016, in 46th European Microwave Conference (EuMC) (London: IEEE), 1568
- Fixsen, D. J. 2009, *ApJ*, **707**, 916
- Hartmann, D., & Burton, W. B. 1997, Atlas of Galactic Neutral Hydrogen
- Kalberla, P. M. W., Burton, W. B., Hartmann, D., et al. 2005, *A&A*, **440**, 775
- Landon, J., Elmer, M., Waldron, J., et al. 2010, *AJ*, **139**, 1154
- Sancisi, R., Fraternali, F., Oosterloo, T., & van der Hulst, T. 2008, *A&ARv*, **15**, 189
- Syed, J., Soler, J. D., Beuther, H., et al. 2022, *A&A*, **657**, A1
- Tavakoli, M. 2012, arXiv:1207.6150
- van Cappellen, W. A., Oosterloo, T. A., Verheijen, M. A. W., et al. 2022, *A&A*, **658**, A146
- Vishwas, A., Parshley, S. C., Gull, G. E., et al. 2022, Proc. SPIE, PC121900G
- Warnick, K. F., & Jeffs, B. D. 2008, *IAWPL*, **7**, 565
- Warnick, K. F., Ruzindana, M., Jeffs, B. D., et al. 2018, in 12th European Conference on Antennas and Propagation (EuCAP 2018) (London: IET), 1
- Wu, Y., Warnick, K. F., & Jin, C. 2013, *ITAP*, **61**, 3026
- Zhang, Y., El-Makadema, A., Danoon, L., & Brown, A. K. 2019, in 2019 International Conference on Electromagnetics in Advanced Applications (ICEAA) (Granada, Spain: IEEE), 958